International Journal of
Environmental Research and Public Health

MDPI

Article

Soot Combustion over Cu–Co Spinel Catalysts: The Intrinsic Effects of Precursors on Catalytic Activity

Chunlin Zhou [1], Xinbo Zhu [1,*], Fei Zhang [1], Xinbao Li [1,*], Geng Chen [1], Zijian Zhou [2] and Guohua Yang [1]

[1] Faculty of Maritime and Transportation, Ningbo University, Ningbo 315211, China
[2] State Key Laboratory of Coal Combustion, School of Energy and Power Engineering, Huazhong University of Science and Technology, Wuhan 430074, China
* Correspondence: zhuxinbo@nbu.edu.cn (X.Z.); lixinbao@nbu.edu.cn (X.L.)

Abstract: In this work, a series of $CuCo_2O_4$-x (x = N, A and C) catalysts were synthesized using different metal salt precursors by urea hydrothermal method for catalytic soot combustion. The effect of $CuCo_2O_4$-x catalysts on soot conversion and CO_2 selectivity in both loose and tight contact mode was investigated. The $CuCo_2O_4$-N catalyst exhibited outstanding catalytic activity with the characteristic temperatures (T_{10}, T_{50} and T_{90}) of 451 °C, 520 °C and 558 °C, respectively, while the CO_2 selectivity reached 98.8% during the reaction. With the addition of NO, the soot combustion was further accelerated over all catalysts. Compared with the loose contact mode, the soot conversion was improved in the tight contact mode. The $CuCo_2O_4$-N catalysts showed better textural properties compared to the $CuCo_2O_4$-A and $CuCo_2O_4$-C, such as higher specific surface areas and pore volumes. The XRD results confirmed that the formation of a $CuCo_2O_4$ crystal phase in all catalysts. However, the CuO crystal phase only presented in $CuCo_2O_4$-N and $CuCo_2O_4$-A. The relative contents of Cu^{2+}, Co^{3+} and O_{ads} on the surface of $CuCo_2O_4$-x (x = N, A and C) catalysts were analyzed by XPS. The $CuCo_2O_4$-N catalyst displayed the highest relative content of Cu^{2+}, Co^{3+} and O_{ads}. The activity of catalytic soot combustion showed a good correlation with the order of the relative contents of Cu^{2+}, Co^{3+} and O_{ads}. Additionally, the $CuCo_2O_4$-N catalyst exhibited lower reduction temperature compared to the $CuCo_2O_4$-A and $CuCo_2O_4$-C. The cycle tests clarified that the copper–cobalt spinel catalyst obtained good stability. In addition, based on the Mars–van Krevelen mechanism, the process of catalytic soot combustion was described combined with the electron transfer process and the role of oxygen species over $CuCo_2O_4$ spinel catalysts.

Keywords: soot combustion; spinel catalyst; precursor; transition metal oxides; catalytic activity

Citation: Zhou, C.; Zhu, X.; Zhang, F.; Li, X.; Chen, G.; Zhou, Z.; Yang, G. Soot Combustion over Cu–Co Spinel Catalysts: The Intrinsic Effects of Precursors on Catalytic Activity. *Int. J. Environ. Res. Public Health* **2022**, *19*, 14737. https://doi.org/10.3390/ijerph192214737

Academic Editor: Fawei Lin

Received: 27 August 2022
Accepted: 28 October 2022
Published: 9 November 2022

1. Introduction

Soot particles are emitted from incomplete combustion of hydrocarbon fuels in diesel engines [1]. Mitigating soot particle emissions from diesel engines has raised much attention due to the negative impact of soot particles on human health and environmental protection [2,3]. A diesel particulate filter (DPF) is the most effective after-treatment technology for soot particles from diesel engines. However, a common issue of pore blockage over DPFs after a period of use should be addressed [4]. One of the most effective measures to improve soot oxidation is to coat the DPF with catalysts and form a catalyzed DPF (CDPF) [5]. CDPFs with highly active catalysts can accelerate soot oxidation and lower the ignition temperatures.

Various catalysts have been proposed and optimized to accelerate the catalytic soot combustion, while Pt-based catalysts have shown superb soot oxidation performance under practical conditions [6,7]. However, due to the high cost of noble metals, transition metal-based catalysts have been intensively studied for catalytic soot oxidation more recently [8]. Copper–cobalt catalysts play an important role as substitutes for noble metals in the field of catalytic soot combustion due to their outstanding redox properties and

thermal stability [9]. Zhang et al. reported that a spinel-type $CuCo_2O_4$ catalyst showed a lower T_{50} temperature (574 °C) of catalytic soot combustion than that of Co_3O_4 catalysts (580 °C) due to its higher relative content of Co^{3+} species [10]. Jampaiah et al. found that a CuCo-MnO_2 catalyst exhibited a lower T_{90} temperature (485 °C) of catalytic soot combustion than that of NiCo-MnO_2 catalysts (513 °C) under the loose contact mode due to more oxygen vacancies and active sites on the catalyst surfaces [11]. Zhang et al. tested the stability of $CuCo_2O_4$ spinel catalysts in four consecutive soot combustion cycles and found that the values of T_{50} for catalytic soot combustion increased from 539 °C to 544 °C, 547 °C and 549 °C, respectively [12].

Recently, the effect of metal salt precursor on the textural and redox properties of catalysts was found to play a key role in catalytic activity and product selectivity [13]. Yang et al. found that the catalytic activity of selective acetylene hydrogenation at 50 °C over the Pd/Al_2O_3 catalyst using acetate as the Pd precursor reached 78.6%, which was 31.1% higher than that using chloride precursors since Cl residuals existed in the form of $PdCl_4^{2-}$, resulting in the decrease of the electron density of Pd atoms [14]. Wang et al. reported that the n-hexadecane conversion over Pt/ZSM-22 catalysts with $Pt(NH_3)_4Cl_2$ precursors was ~9.1% higher compared to that over catalysts using $Pt(NO_3)_2$ and H_2PtCl_6 as the precursors due to the higher platinum dispersion [15]. Yun et al. found that the Ni/Al_2O_3 catalyst using acetate salt precursors achieved the highest activity (85.6%) in the steam reforming of acetic acid at 450 °C, while the catalytic activity of the catalyst prepared from chloride salts was only 38.7% [16]. These results indicated that the role of precursors should be preferentially considered during the designing and preparation of heterogeneous catalysts.

In this work, copper–cobalt spinel oxides were prepared with a urea hydrothermal method using different copper and cobalt precursors (nitrate, chloride and acetate). The physicochemical properties of these catalysts were characterized by N_2 adsorption–desorption, X-ray diffraction (XRD), scanning electron microscopy (SEM), X-ray photoelectron spectroscopy (XPS), temperature-programed reduction of H_2 (H_2-TPR) and temperature-programed desorption of O_2 (O_2-TPD). The catalytic activity of soot combustion was investigated by temperature-programed oxidation (TPO) experiments under various reaction conditions.

2. Experimental Study

2.1. Catalyst Preparation

In this work, a series of $CuCo_2O_4$-x catalysts was synthesized by urea hydrothermal methods with different precursors, where x represented the types of copper and cobalt precursors, e.g., the nitrates (N), acetate (A) and chloride (C), respectively. All chemicals used were of analytical reagent grade and purchased from Macklin Co., Ltd. (Shanghai, China). Taking $CuCo_2O_4$-N as an example, 0.02 mol $Cu(NO_3)_2{\cdot}3H_2O$, 0.04 mol $Co(NO_3)_3{\cdot}6H_2O$ and 0.06 mol CH_4N_2O were dissolved in 100 mL of deionized water and stirred for 1 h at room temperature. Afterwards, the mixed solution was transferred to a polytetrafluoroethylene-lined high pressure reactor placed in a thermostat at 150 °C for hydrothermal reaction. After 12 h, the resulting solution was filtered to obtain a precipitate. The precipitate was then washed three times with deionized water and dried in an oven at 110 °C overnight. Finally, the precipitate was calcined in a muffle furnace at 700 °C for 6 h and sieved to 40–60 meshes. The prepared catalysts were denoted as $CuCo_2O_4$-N, $CuCo_2O_4$-A and $CuCo_2O_4$-C, respectively.

2.2. Catalyst Characterizations

N_2 adsorption–desorption analysis was conducted at 77 K to determine the specific surface area, pore size distribution and average pore diameter of the catalysts using TriStar II 3020 (Micromeritics, Norcross, GA, USA). The specific surface areas were calculated using the Brunauer–Emmett–Teller (BET) method. Total pore volume and pore size distribution were calculated via the Barrett–Joyne–Halenda (BJH) method at the relative pressure of $p/p_0 = 0.99$. The crystal structure of catalysts was observed by X-ray diffraction (XRD) using a diffractometer system (D-Max 2000, Rigaku, Tokyo, Japan) with Cu-Kα radiation operating at 40 kV and 30 mA. All catalysts were scanned in the range of 10° to 80° with a step size of 0.02°. A scanning electron microscopy (SEM) instrument (JSM-7001F, JEOL, Tokyo, Japan) was used to observe the surface morphology of catalysts at an accelerating voltage of 10 kV. The X-ray photoelectron spectra (XPS) were measured with Thermo Escalab 250Xi equipment with monochromatic Al-Ka X-ray radiation at 150 W. All binding energies were calibrated using the C 1s photoelectron peak at 284.8 eV. The redox properties of all catalysts were analyzed using the temperature-programed reduction of the H_2 (H_2-TPR) apparatus (Autochem II 2920, Micromeritics, Norcorss, GA, USA). To remove impurities, 16 mg catalysts were pretreated at 250 °C for 1 h and cooled down to room temperature before each test. Then, the catalysts were heated from room temperature to 800 °C at a heating rate of 10 °C·min^{-1} in a 30 mL·min^{-1} feeding gas flow (10 vol.% H_2/Ar). The amount of H_2 consumption was calculated based on the H_2-TPR profiles. The profiles of the temperature-programed desorption of O_2 (O_2-TPD) were performed using the same apparatus as that for H_2-TPR. Before the measurement, 200 mg of catalysts were pretreated in an He stream at 200 °C for 1 h and cooled down to room temperature. Then, the adsorption of O_2 was conducted at 70 °C for 1 h in a gas mixture of 3 vol.% O_2/He (30 mL·min^{-1}). Subsequently, the sample was purged by a flowing pure He stream to remove excessive and weakly adsorbed O_2. Finally, the sample was heated to 800 °C with a heating rate of 10 °C·min^{-1} in a pure He flow (30 mL·min^{-1}), and the desorption profile was recorded.

2.3. Experimental System

Figure 1 shows a schematic diagram of the experimental setup. The catalytic activity of the $CuCo_2O_4$-x (x = N, C and A) catalysts was evaluated by temperature-programed oxidation (TPO) experiments. Printex-U (Degussa, with the size of 20–30 nm) was used as the model soot in this study. For each test, 180 mg of catalyst powder was mixed with 20 mg of soot in loose (mixing with a spatula for 5 min) or tight (grinding in an agate mortar for 5 min) contact mode. Then, the resulting soot–catalyst mixtures (200 mg) were mixed with 400 mg of inert silica (40–60 meshes) for another 5 min to avoid the formation of hot spots during the reaction. The experimental procedure was as follows: Firstly, the mixture of catalyst and inert silica after reaction was collected from the quartz tube and then placed in an agate mortar. Secondly, 20 mg of soot was mixed with the obtained mixture of the catalyst and inert silica after reaction in loose contact mode. Finally, the above obtained mixture of soot, catalyst and inert silica was filled back into the quartz tube for next catalytic soot combustion reaction cycle. The reaction temperature was increased from 50 °C to 700 °C at a heating rate of 5 °C·min^{-1}.

All gas streams from the gas cylinders were regulated by mass flow controllers (Sevenstars D07-B, Beijing, China). The mixed gases (10 vol.% O_2 with balanced N_2) were fed into the reactor at the flow rate of 200 mL·min^{-1} during the TPO experiment. In addition, 1000 ppm NO was added into the feeding gas to investigate the effect of NO on catalytic soot combustion when necessary. The outlet concentrations of CO and CO_2 were monitored online using an infrared (IR) gas analyzer (GXH-3010/3011AE, Huayun, Beijing, China) with the accuracy of ±3%. The temperatures at which 10%, 50% and 90% of the soot was oxidized (denoted as T_{10}, T_{50} and T_{90}, respectively) were recorded as indicators of the

catalytic activity. Soot conversion (denoted as α) and CO_2 selectivity (denoted as S_{CO_2}) were calculated by integrating the CO and CO_2 concentration curves with time as follows:

$$\alpha\ (\%) = \frac{\int_0^t ([CO_2]_{out} + [CO]_{out})dt}{M} \times 100\% \quad (1)$$

$$S_{CO_2}(\%) = \frac{\int_0^t [CO]_{out}\,dt}{\int_0^t ([CO_2]_{out} + [CO]_{out})dt} \times 100\% \quad (2)$$

where $[CO_2]_{out}$ and $[CO]_{out}$ are the real-time concentrations of CO and CO_2 at the reactor outlet, respectively, and M is the weight of the initially packed soot.

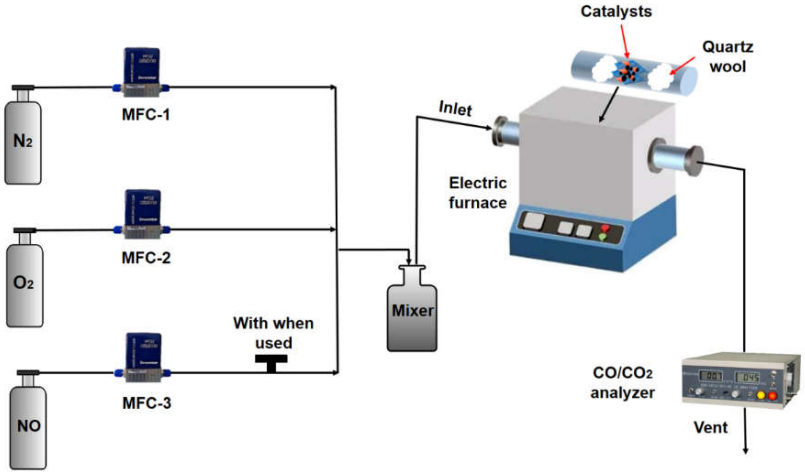

Figure 1. Schematic diagram of the experimental setup.

3. Results and Discussion

3.1. Textural Properties of the Catalysts

The specific surface area (S_{BET}), pore volume and pore size of $CuCo_2O_4$-*x* (*x* = N, A and C) catalysts are obtained with a N_2 adsorption–desorption experiment (Table 1). The $CuCo_2O_4$-N catalyst shows the largest specific surface area of 2.1 $m^2 \cdot g^{-1}$, followed by $CuCo_2O_4$-A (2.0 $m^2 \cdot g^{-1}$) and $CuCo_2O_4$-C (1.2 $m^2 \cdot g^{-1}$). The pore volumes of $CuCo_2O_4$-N, $CuCo_2O_4$-A and $CuCo_2O_4$-C catalysts are 4.5 $mm^3 \cdot g^{-1}$, 4.3 $mm^3 \cdot g^{-1}$ and 2.5 $mm^3 \cdot g^{-1}$, respectively. The specific surface area and pore volume of the $CuCo_2O_4$ catalysts prepared with nitrate and acetate metal salt show no significant differences, while the specific surface area and pore volume of $CuCo_2O_4$-C catalyst dramatically decreases. Yu et al. also reported the formation of hydrochloric acid from chloride salts during calcination, which may inhibit the formation of developed pore systems and negatively affect the specific surface area [16]. Compared with conventional metal oxides and supported catalysts, the specific surface area, pore volume and average pore size of the prepared Cu–Co spinel catalysts are rather low. The results could be ascribed to the formation of the well-crystallized spinel structure under high calcination temperature (700 °C) [12,17].

Table 1. Textural properties of the $CuCo_2O_4$-*x* (*x* = N, A and C) catalysts.

Catalysts	S_{BET} ($m^2 \cdot g^{-1}$)	Pore Volume ($mm^3 \cdot g^{-1}$)	Average Pore Diameter (nm)	Average Crystal Size (nm) *
$CuCo_2O_4$-N	2.1	4.5	8.3	38.0
$CuCo_2O_4$-A	2.0	4.2	8.6	38.3
$CuCo_2O_4$-C	1.2	2.5	8.5	38.8

* Calculated by the Scherrer equation, based on the characteristic peak of $CuCo_2O_4$ (3 1 1) crystal face located at the 2θ of 36.8°.

Figure 2 shows the XRD patterns of the $CuCo_2O_4$-*x* (*x* = N, A and C) catalysts. Sharp and intense diffraction peaks of copper–cobalt spinel phases are observed for all samples, suggesting the formation of well-crystallized structures at high calcination temperature of 700 °C. The diffraction peaks observed at 19.1°, 31.4°, 36.9°, 45.1°, 56.0°, 59.6°, 68.9° and 77.5° are attributed to tetragonal spinel crystalline of $CuCo_2O_4$ (JCPDS No. 01-1155) [18]. Meanwhile, metal oxide CuO phase (JCPDS No. 80-0076) is observed at 35.6°, 48.6° and 61.7° over $CuCo_2O_4$-N and $CuCo_2O_4$-A catalysts [19]. No distinct CuO phase is found on the $CuCo_2O_4$-C catalyst. Based on the characteristic peak of $CuCo_2O_4$ (3 1 1) crystal face, the crystal size of the $CuCo_2O_4$-*x* catalysts were calculated using the Scherrer equation (Table 1). The crystal size of the $CuCo_2O_4$-N catalyst (38.0 nm) is slightly smaller than that of $CuCo_2O_4$-A and $CuCo_2O_4$-C catalysts. Wen et al. also found that the Cl^- coordination anion was an important contributor to the formation of larger clusters of $CuCo_2O_4$ [20].

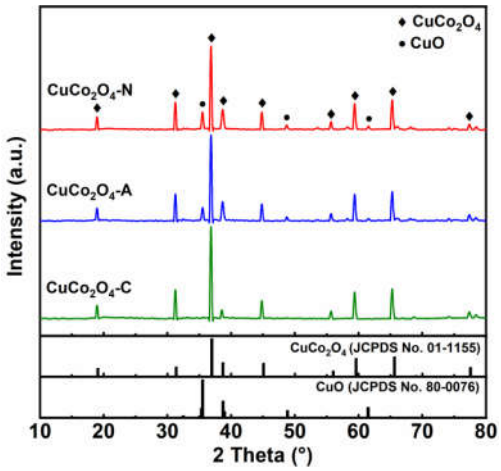

Figure 2. XRD patterns of the $CuCo_2O_4$-*x* (*x* = N, A and C) catalysts.

Figure 3 shows the representative SEM images of the $CuCo_2O_4$-*x* (*x* = N, A and C) catalysts. The $CuCo_2O_4$-N catalyst exhibits a sheetlike morphology with tiny spherical particles on its surface. The stacking of spherical particles and its sheetlike morphologies promote the formation of porous structures (Figure 3a). The phenomenon of particle agglomeration is exhibited over the $CuCo_2O_4$-A and $CuCo_2O_4$-C catalyst (Figure 3c,e). As shown in Figure 3b, the spherical particles are dispersed on the sheetlike morphology and formed a dendritic structure. However, tiny spherical particles are hardly generated on the surfaces of the $CuCo_2O_4$-A and $CuCo_2O_4$-C catalysts (Figure 3d,f), while the agglomeration of bulk particles might have resulted in the blockage of the pore systems. These tiny spherical particles can improve the contact between the catalyst and soot particles, which can facilitate the utilization of the catalyst active sites for catalytic soot combustion. The particle sizes of $CuCo_2O_4$-A and $CuCo_2O_4$-C catalysts increased obviously compared to the $CuCo_2O_4$-N catalysts.

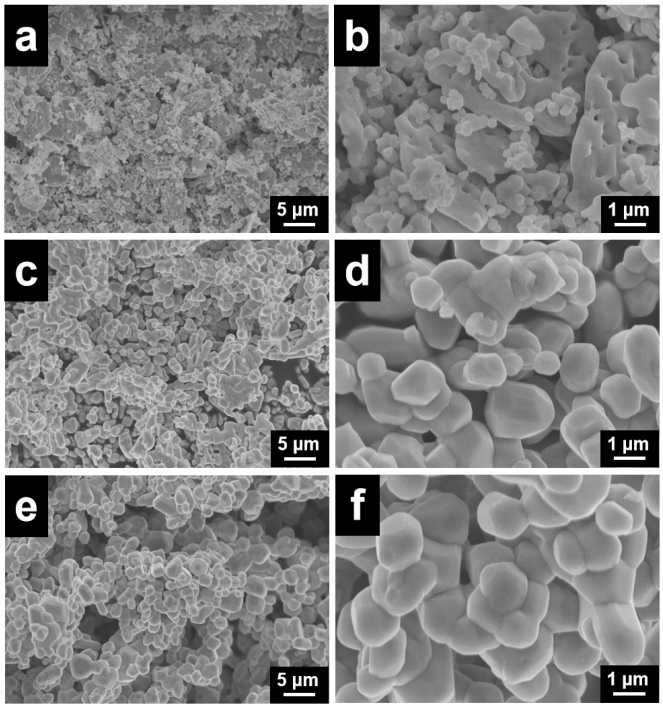

Figure 3. SEM images of the $CuCo_2O_4$-N (**a**,**b**), $CuCo_2O_4$-A (**c**,**d**) and $CuCo_2O_4$-C (**e**,**f**) catalysts.

3.2. Redox Properties of the Catalysts

The Co 2p spectra of the $CuCo_2O_4$-*x* (*x* = N, A and C) catalysts are shown in Figure 4a. The peaks of Co $2p_{3/2}$ and Co $2p_{1/2}$ are observed in the range of 776.0–784.0 eV and 792.0–800.0 eV, respectively [21]. The peaks between 784.0–792.0 eV and 800.0–808.0 eV are attributed to the satellite peaks of Co^{2+} [22,23]. The Co^{3+} and Co^{2+} signals are obtained after the deconvolution of the Co $2p_{3/2}$ and Co $2p_{1/2}$ spectra. The peaks centered at 779.7 eV and 794.8 eV correspond to the Co^{3+} species, while the peaks located at 780.8 eV and 796.4 eV belong to the Co^{2+} species [24]. The Cu 2p spectra of all catalysts are also given in Figure 4b. The peaks observed at 932.6 eV belong to the reduced Cu species (Cu^+ or Cu^0), while the prominent signals at 934.6 eV are ascribed to the Cu^{2+} species [25]. Additionally, the satellite peaks between 937.0 eV to 946.0 eV also confirm the existence of divalent Cu species [19]. Figure 4c shows the Cu LMM Auger spectra of all $CuCo_2O_4$ catalysts. The peaks at the kinetic energy of 912.6 eV correspond to the Cu^+ species, while the peaks at 917.8 eV are attributed to the Cu^{2+} species [26]. However, Cu^0 species are not observed on the Cu LMM Auger spectrum. These results suggest that the reduced copper species on the surfaces of $CuCo_2O_4$-*x* (*x* = N, A and C) catalysts mainly exists as Cu^+. The de-convoluted XPS signals of O 1s are shown in Figure 4d. Two types of oxygen species present on the surface of the $CuCo_2O_4$ catalysts. The peaks around 529.8 eV correspond to the lattice oxygen species (O_{latt}), while the peaks around 531.4 eV are attributed to the adsorbed oxygen species (O_{ads}) [27].

The relative contents of Cu^{2+} and Co^{3+} on the surface of $CuCo_2O_4$-*x* catalysts are given in Table 2. The highest relative content of Co^{3+}/Co_{total} (38.4%) is obtained over the $CuCo_2O_4$-N catalyst, followed by $CuCo_2O_4$-A (35.1%) and $CuCo_2O_4$-C (33.8%). Moreover, the highest relative content of Cu^{2+}/Cu_{total} is also achieved over the $CuCo_2O_4$-N catalyst (51.7%), followed by $CuCo_2O_4$-A (48.2%) and $CuCo_2O_4$-C (47.8%). The highest relative content of $O_{ads}/(O_{ads} + O_{latt})$ (46.8%) is found over the $CuCo_2O_4$-N catalyst, followed by $CuCo_2O_4$-A (37.2%) and $CuCo_2O_4$-C (36.5%) (Table 2). The adsorbed oxygen species were more chemically active than lattice oxygen in catalytic soot combustion, indicating a better soot conversion performance over the $CuCo_2O_4$-N catalyst with more O_{ads} species [28].

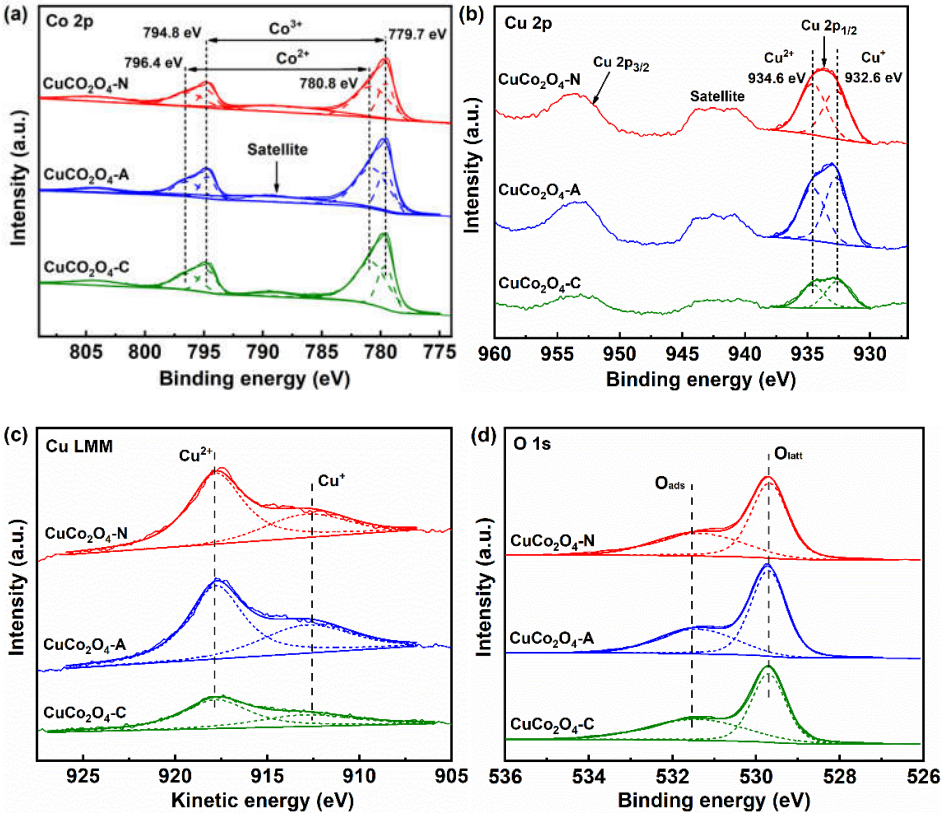

Figure 4. XPS spectra of the $CuCo_2O_4$-*x* (*x* = N, A and C) catalysts: (**a**) Co 2p; (**b**) Cu 2p; (**c**) Cu LMM; (**d**) O 1s.

Table 2. Redox properties of the $CuCo_2O_4$-*x* (*x* = N, A and C) catalysts.

Catalysts	Co^{3+}/Co_{total} (%)	Cu^{2+}/Cu_{total} (%)	$O_{ads}/(O_{ads}+O_{latt})$ (%)	H_2 Consumption (mmol·g^{-1})	O_2 Uptake (μmol·g^{-1})
$CuCo_2O_4$-N	38.4	51.7	46.8	13.4	41.2
$CuCo_2O_4$-A	35.1	48.2	37.2	13.6	27.1
$CuCo_2O_4$-C	33.8	47.8	36.5	14.5	25.6

For the $CuCo_2O_4$-N catalyst, two reduction peaks are observed (Figure 5). The first reduction peak in the range of 150–200 °C is attributed to the reduction of aggregated CuO, while the second peak between 200 °C and 250 °C can be ascribed to the reduction of Cu–Co mixed oxides [29]. The $CuCo_2O_4$-A catalyst exhibits shoulder peaks at 200–300 °C, the first reduction peak (244 °C) corresponds to the reduction of Cu–Co mixed oxides, and the latter reduction peak at 278 °C represents the reduction of Co^{3+} to Co^{2+} [30]. The $CuCo_2O_4$-C catalyst also shows two major peaks between 250 °C and 350 °C. The weak reduction peak at 299 °C is ascribed to the reduction of Co^{3+} to Co^{2+}, while the reduction peak at 331 °C represents the reduction of Co^{2+} to Co^{0+} [31]. These results suggest that $CuCo_2O_4$-N catalyst has better reducibility at relatively low temperatures. The amount of H_2 consumption was in the order of $CuCo_2O_4$-C > $CuCo_2O_4$-A > $CuCo_2O_4$-N. Although the $CuCo_2O_4$-C catalysts show the higher H_2 consumption (14.5 mmol·g^{-1}), the H_2 consumption of the $CuCo_2O_4$-N catalyst is likely mainly concentrated in the low temperature range (150–250 °C). Therefore, the distribution of oxygen species was further investigated.

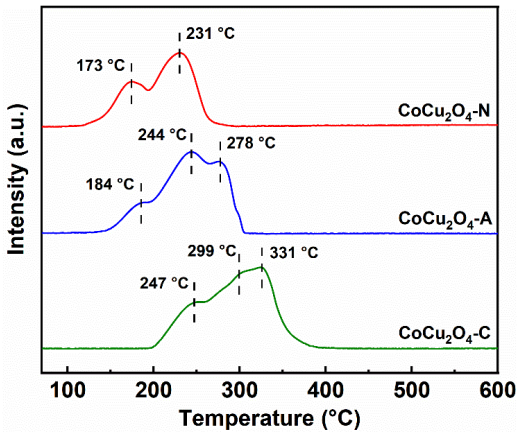

Figure 5. H_2-TPR profiles of the $CuCo_2O_4$-x (x = N, A and C) catalysts.

Figure 6a shows the O_2-TPD profiles of the $CuCo_2O_4$-x (x = N, A and C) catalysts. The oxygen desorption peaks below 500 °C belong to adsorbed oxygen species (e.g., O_2, O_2^- and O^-, labeled as α-O_2) [32], while the oxygen desorption peaks between 600 °C and 850 °C belong to the lattice oxygen species (O^{2-}, labeled as β-O_2) [33]. Figure 6b shows the enlarged O_2-TPD profiles in the temperature range of 50 °C to 550 °C. The oxygen desorption peaks within 50–300 °C and 300–500 °C correspond to the physically adsorbed oxygen (α_1-O_2) and chemically adsorbed oxygen (α_2-O_2) species, respectively [34,35]. Generally, the adsorption of oxygen followed the procedure of $O_2 \rightarrow O_2^- \rightarrow O^- \rightarrow O^{2-}$ [27]. The $CuCo_2O_4$-N catalyst shows an extra oxygen desorption peak in the temperature range of 200 °C to 250 °C compared to the $CuCo_2O_4$-A and $CuCo_2O_4$-C. The extra oxygen desorption peak could be attributed to physically adsorbed oxygen (α_1-O_2), indicating that the catalysts had better oxygen mobility [36]. Similarly, Li et al. also reported that the $CuCo_2O_4$ and $NiCo_2O_4$ catalysts showed an extra oxygen desorption peak in the temperature range of 200 °C to 250 °C compared to the $ZnCo_2O_4$. The catalytic performance of $CuCo_2O_4$ and $NiCo_2O_4$ catalysts were found to be far superior to that of $ZnCo_2O_4$ in toluene combustion [7]. The desorption amount of α_1-O_2 and α_2-O_2 species were calculated according to the desorption peaks in the O_2-TPD profiles. As shown in Table 2, the amount of O_2 desorption was in the order of $CuCo_2O_4$-N (41.2 μmol·g^{-1}) > $CuCo_2O_4$-A (27.1 μmol·g^{-1}) > $CuCo_2O_4$-C (25.6 μmol·g^{-1}), which confirms the existence of more adsorbed oxygen species over the $CuCo_2O_4$-N catalyst.

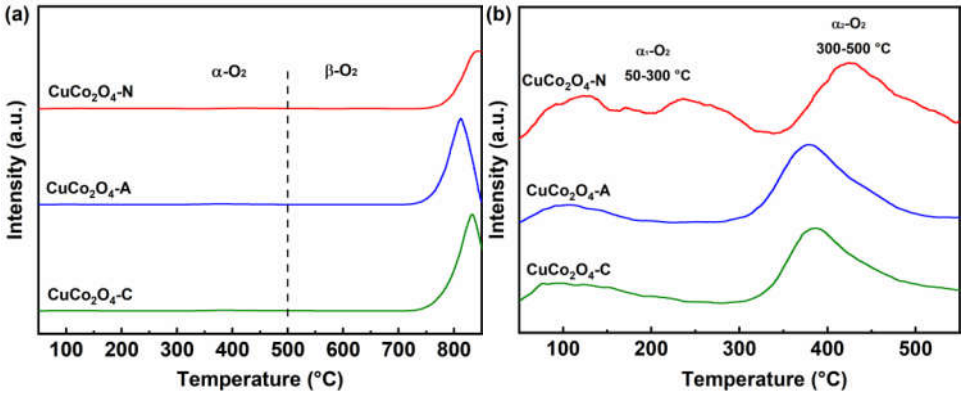

Figure 6. O_2-TPD profiles (**a**) and the enlarged O_2-TPD profiles in the temperature range of 50 °C to 550 °C (**b**) of the $CuCo_2O_4$-x (x = N, A and C) catalysts.

3.3. Activity of $CuCo_2O_4$-x for Soot Conversion

3.3.1. Soot Conversion in O_2/N_2

The catalytic activity of $CuCo_2O_4$-*x* (*x* = N, A and C) catalysts for soot combustion were studied using a TPO experiment under the loose contact mode. Firstly, the soot conversion was investigated under the carrier gases of 10 vol.% O_2 balanced with N_2. The characteristic temperatures (T_{10}, T_{50} and T_{90}) of soot conversion are 530 °C, 586 °C and 614 °C, respectively in the absence of a catalyst, which is much higher than those in the presence of the $CuCo_2O_4$ catalysts (Figure 7 and Table 3). The catalysts prepared with different metal salt precursors exhibit different catalytic activity in the soot conversion. Among them, the $CuCo_2O_4$-N catalyst achieves the highest soot conversion, while the values of T_{10}, T_{50} and T_{90} are 451 °C, 520 °C and 558 °C, respectively. The T_{50} values for the $CuCo_2O_4$-*x* (*x* = N, A and C) catalysts followed the order of $CuCo_2O_4$-N (520 °C) < $CuCo_2O_4$-A (539 °C) < $CuCo_2O_4$-C (550 °C) < no catalysts (586 °C). The CO_2 selectivity is also improved remarkably from 81.8% over the $CuCo_2O_4$-C to almost 100% over the $CuCo_2O_4$-N catalysts.

Table 3. Catalytic activity of the $CuCo_2O_4$-*x* (*x* = N, A and C) catalysts for soot combustion under loose contact mode in 10 vol.% O_2 with balanced N_2.

Catalysts	10 vol.% O_2/N_2			
	T_{10} (°C)	T_{50} (°C)	T_{90} (°C)	S_{CO_2} (%)
$CuCo_2O_4$-N	451	520	558	98.8
$CuCo_2O_4$-A	496	539	569	95.0
$CuCo_2O_4$-C	504	550	594	81.8
No catalysts	530	586	615	58.7

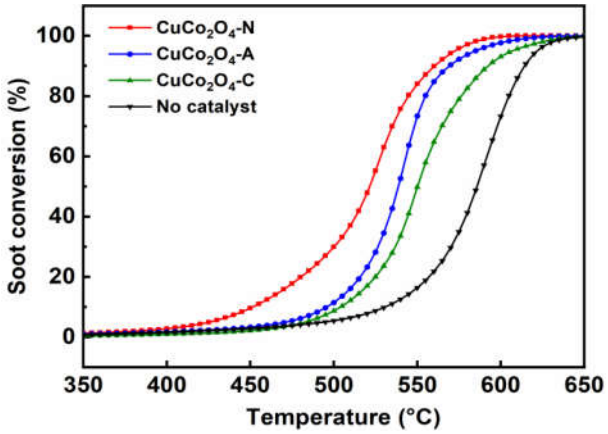

Figure 7. Soot conversion over the $CuCo_2O_4$-*x* (*x* = N, A and C) catalysts under loose contact mode under the carrier gas of 10 vol.% O_2 with balanced N_2.

The $CuCo_2O_4$-N and $CuCo_2O_4$-A catalysts exhibit larger specific surface area and pore volume compared to the $CuCo_2O_4$-C catalyst. It is widely recognized that a larger specific surface area could facilitate the contact between gaseous reactants (e.g., O_2, NO and NO_2) and the catalyst [37,38]. SEM images further confirmed the generation of more developed pore structure systems of the $CuCo_2O_4$-N catalyst compared to the $CuCo_2O_4$-A and $CuCo_2O_4$-C catalysts. Fang et al. reported that a perovskite-type macro/mesoporous $La_{1-x}K_xFeO_{3-\delta}$ catalysts with large specific surface area and pore volume could improve the utilization of catalytic sites in the soot combustion reaction [39]. Furthermore, the presence of an appropriate amount of single metal oxide CuO on the $CuCo_2O_4$ surface could contribute to the crystal lattice distortion of the spinel phase and promote the formation of a defect structure, thereby improving the catalytic activity of the soot combustion reaction [40].

The redox properties of $CuCo_2O_4$-*x* catalysts played a crucial role in catalytic soot combustion. The higher relative content of Co^{3+}/Co_{total} (38.4%) and Cu^{2+}/Cu_{total} (51.7%) obtained over $CuCo_2O_4$-N catalysts were much higher compared to the $CuCo_2O_4$-A (35.1% and 48.2%) and $CuCo_2O_4$-C (33.8% and 47.8%), respectively. Spinel-type $CuCo_2O_4$ catalysts possessed outstanding redox properties since the synergistic effects between Co^{3+} and Cu^{2+} species could enhance the adsorption-activation properties of oxygen species for soot conversion [41]. Abundant Co^{3+} species would increase the anionic defects on catalyst surfaces, leading to the formation of more oxygen vacancies [42]. Zhang et al. reported that the presence of Cu^{2+} species induced structural defects on cobalt oxide and weakened the Co-O bonds, which could facilitate the activation of oxygen and improve the reducibility of $CuCo_2O_4$ [43]. In addition, the $CuCo_2O_4$-N catalysts showed the highest relative content of $O_{ads}/(O_{ads} + O_{latt})$ (46.8%) compared to the $CuCo_2O_4$-A (37.2%) and $CuCo_2O_4$-C (36.5%). The O_{ads} species possessed better mobility than O_{latt} species and could participate in catalytic soot combustion via the contact points between catalyst pellets and soot particulates [35].

The lower reduction peaks temperature proved that the $CuCo_2O_4$-N catalysts (173 °C) has excellent low temperature reduction performances compared to the $CuCo_2O_4$-A (184 °C) and $CuCo_2O_4$-C (247 °C). The total H_2 consumption amount of the $CuCo_2O_4$-N catalysts (13.4 mmol·g^{-1}) was slightly lower than that of $CuCo_2O_4$-A (13.6 mmol·g^{-1}) and $CuCo_2O_4$-C (14.5 mmol·g^{-1}). The $CuCo_2O_4$-N catalyst possessed more adsorbed oxygen species (41.2 μmol·g^{-1}) compared to the $CuCo_2O_4$-A (27.1 μmol·g^{-1}) and $CuCo_2O_4$-C (25.6 μmol·g^{-1}). It was suggested that the $CuCo_2O_4$-N catalysts could release more adsorbed oxygen species below 500 °C [44]. Compared with lattice oxygen species, adsorbed oxygen species were more important in soot conversion due to their better oxygen mobility [45]. He et al. also reported that the adsorbed oxygen species released at low temperatures were more important than lattice oxygen species since the lattice oxygen species could be activated and released only at high temperatures [35]. Lower reduction temperature and abundant adsorbed oxygen species may be crucial factors for soot conversion over the $CuCo_2O_4$-N catalyst at lower temperature.

3.3.2. Soot Conversion in $NO/O_2/N_2$

NO is one of the main components in diesel engine exhaust and has a great effect on soot conversion. Therefore, soot conversion was investigated over the $CuCo_2O_4$-*x* (*x* = N, A and C) catalysts in the presence of 1000 ppm NO (Figure 8 and Table 4). The addition of NO resulted in lower T_{10}, T_{50} and T_{90} values regardless of the presence of a catalyst. The T_{50} values for the $CuCo_2O_4$-*x* (*x* = N, A and C) catalysts also follow the order of $CuCo_2O_4$-N (414 °C) < $CuCo_2O_4$-A (458 °C) < $CuCo_2O_4$-C (485 °C) < no catalysts (575 °C).

Table 4. Catalytic activity of the $CuCo_2O_4$-*x* (*x* = N, A and C) catalysts for soot combustion under the loose contact mode with 1000 ppm NO.

Catalysts	T_{10} (°C)	T_{50} (°C)	T_{90} (°C)	S_{CO_2} (%)
$CuCo_2O_4$-N	349	414	482	96.6
$CuCo_2O_4$-A	381	458	494	94.3
$CuCo_2O_4$-C	392	485	534	79.7
No catalysts	496	575	615	43.6

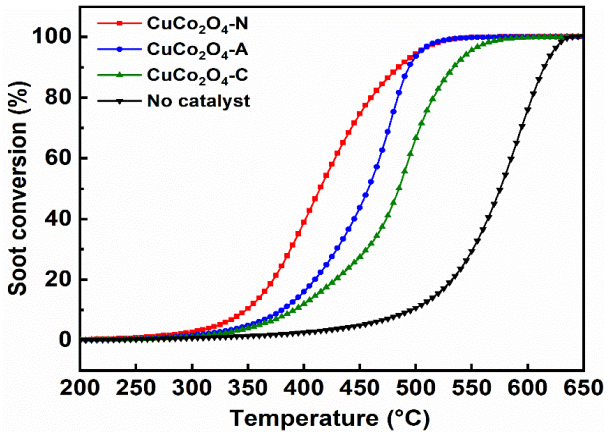

Figure 8. Soot conversion of the $CuCo_2O_4$-*x* (*x* = N, A and C) catalysts under the loose contact mode with 1000 ppm NO.

Using $CuCo_2O_4$-N as an example, the T_{50} value decreases from 520 °C to 414 °C with NO addition, while the CO_2 selectivity also decreases from 98.8% to 96.6%. NO could be oxidized with O_2 to form NO_2 in gas phase (Reaction (3)) [46]. NO could be also adsorbed on the surface of $CuCo_2O_4$-N catalyst and then oxidized by the active oxygen to form NO_2 species, while could promote the formation of surface oxygen vacancies (Reaction (4)). NO_2 is a stronger oxidant and participate in catalytic soot combustion as a mobile gaseous oxidant [46]. Possible pathways for the reaction of NO_2 with soot are shown in Reaction (5) [47]. NO_2 could attack the soot on the surface, resulting in the generation of CO and NO, while CO was eventually oxidized by O_2 to CO_2, with NO again participating in the NO_x-assisted catalytic soot combustion [37]. However, the slight decrease in CO_2 selectivity could be attributed to the rapid oxidation of soot by NO_2, resulting in the incomplete oxidation of soot to CO [48].

$$2NO + O_2 \rightarrow 2NO_2 \quad (3)$$

$$NO + O^* \rightarrow NO_2 + O_v \quad (4)$$

$$NO_2 + C(Soot) \rightarrow CO + NO \quad (5)$$

where O* represents the active oxygen species, O_v represents the surface oxygen vacancy and C(Soot) represents the soot particulate.

3.3.3. Effect of the Contact Mode

The contact mode between the catalyst and soot could greatly affect the activity of soot conversion [41]. The soot conversion and CO_2 selectivity were investigated under both loose and tight contact modes over the $CuCo_2O_4$-N catalyst (Figure 9 and Table 5). Under the tight contact mode, soot conversion is accelerated at lower temperatures regardless of the presence of NO compared to the loose contact mode, while the CO_2 selectivity reaches up to 100%. The increase of catalyst–soot contact points in the tight contact mode could contribute to better utilization of active sites on the catalyst surface compared to the loose contact mode [4,27]. Machida et al. found that the utilization/transfer of lattice oxygen species was more efficient under the tight contact mode. Besides, the case of "O_2 slip" may be decreased in the tight contact mode, which increases the utilization of the released oxygen species to the soot combustion [49].

Table 5. Catalytic activity of the $CuCo_2O_4$-N catalysts for soot combustion under the loose and tight contact modes.

Contact Mode	T_{10} (°C)	T_{50} (°C)	T_{90} (°C)	S_{CO_2} (%)
Loose contact	451	520	558	98.8
Loose contact + NO	349	414	482	96.6
Tight contact	385	428	499	100
Tight contact + NO	339	394	448	100

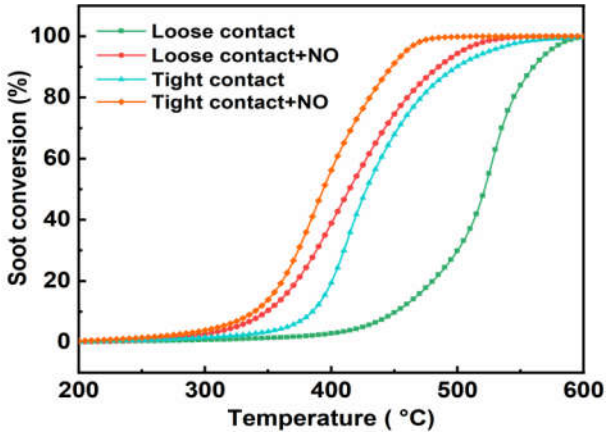

Figure 9. Soot conversion over the $CuCo_2O_4$-N catalyst under the loose and tight contact modes.

3.3.4. Stability Test

The stability test of $CuCo_2O_4$-N catalysts was conducted for four consecutive cycles of soot combustion. As shown in Figure 10, the characteristic temperatures (T_{10}, T_{50} and T_{90}) increased slightly with the increase in the number of cycles of soot combustion. For examples, the values of T_{50} for catalytic soot combustion for each cycle are 520 °C, 524 °C, 526 °C and 528 °C, respectively. Figure 11 shows the deconvoluted XPS spectra of O 1s for the $CuCo_2O_4$-N catalyst after four consecutive cycles of soot combustion. The relative content of $O_{ads}/(O_{ads} + O_{latt})$ of $CuCo_2O_4$-N catalyst decreases from 46.8% to 40.6% (Table 6). The slight decrease in soot catalytic activity may be due to the minor attenuation of the relative content of $O_{ads}/(O_{ads} + O_{latt})$. Chen et al. also reported the catalytic soot performance of Ag/Co_3O_4 and found that the decrease in adsorbed oxygen species was an important reason for the decrease of catalytic soot combustion [50].

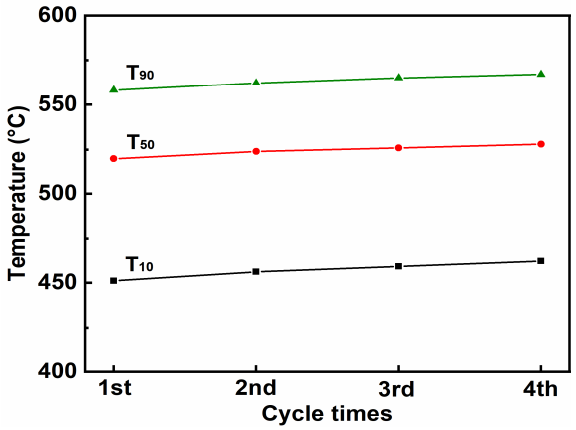

Figure 10. Stability of $CuCo_2O_4$-N catalyst in cycle tests for soot combustion.

Table 6. XPS parameters of $CuCo_2O_4$-N catalyst before and after reaction.

Catalysts	$O_{ads}/(O_{ads} + O_{latt})$ (%)
$CuCo_2O_4$-N (fresh)	46.8
$CuCo_2O_4$-N (used)	40.6

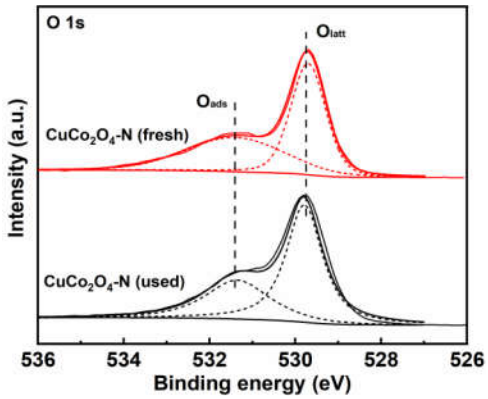

Figure 11. XPS spectra of O 1 s of $CuCo_2O_4$-N catalyst before and after reaction.

4. Reaction Mechanisms for Catalytic Soot Combustion

The potential reaction pathways of catalytic soot combustion over $CuCo_2O_4$ were discussed. The excellent catalytic soot combustion of the copper–cobalt spinel catalyst performance depended on the redox properties of the catalysts [41]. The interactions between Cu and Co species in the $CuCo_2O_4$ catalyst played a crucial role in the redox reactions. Previous studies showed that the redox pairs of Cu^{2+}/Cu^{+} and Co^{3+}/Co^{2+} were involved in the electron transfer process from Co^{3+} to Cu^{2+} within the Cu^{2+}–O–Co^{3+} connections in the copper–cobalt spinel catalysts [31,51]. The Cu^{2+}–O–Co^{3+} connections could bridge the oxygen transfer within the structure and reduce the redox potential of the Cu species, which ensures the improvement of reducibility for both Cu and Co oxides in the Cu–Co catalysts (Reaction (6)), facilitating the NO_x-assisted mechanism in the soot combustion reaction [46].

$$Cu^{2+} / Cu^{+} \underset{O^{2-}/O^{-}}{\overset{2e^{-}}{\rightleftharpoons}} Co^{3+} / Co^{2+} \quad (6)$$

Catalytic soot combustion over the copper–cobalt spinel catalyst followed the Mars–van Krevelen (MvK) mechanism, in which the abundance of active oxygen species directly determined the performance of catalytic soot combustion [5]. At the beginning of soot conversion, plenty of active oxygen species on the catalyst surface would come into contact with the soot, resulting in soot combustion at a relatively low temperature and the subsequent formation of oxygen vacancies (O_v) (Reaction (7)) [49]. As the reaction proceeded, the consumed reactive oxygen species could be replenished in two ways. Firstly, the reduction of high-valence Cu^{2+} and Co^{3+} to low-valence Cu^{+} and Co^{2+} released the oxygen species and formed oxygen vacancies, making the surface of the catalyst ready for the oxygen species adsorption from the gas phase ($O_{2(gas)}$) and accelerating the conversion of the gas phase oxygen species to the adsorbed oxygen species (Reactions (8) and (9)) [7]. The relative content of adsorbed oxygen species of the used $CuCo_2O_4$-N catalysts (40.6%) was significantly decreased compared to the fresh $CuCo_2O_4$-N catalysts (46.8%), and the activity of soot conversion was also decreased. The adsorbed oxygen species played a crucial role in catalytic soot combustion, which could be transformed to active oxygen species such as O_2, O_2^- and O^- (Reactions (10)–(12)) [52]. Moreover, some lattice oxygen species took over the oxygen vacancies and were transferred into adsorbed oxygen species. The adsorbed oxygen species were spilled over to the soot particle surface and further

contributed to the soot combustion reaction [35]. All these active oxygen species could directly participate in catalytic soot combustion reaction via the contact points between catalysts and soot particulates to form CO and CO_2 [37]. In addition, the released active oxygen species for the conversion of NO oxidation of NO_2 [42]. Moreover, the Cu^+ and Co^{2+} species were reoxidized to Cu^{2+} and Co^{3+} due to the replenishment of oxygen vacancies and participation in catalytic soot combustion (Reaction (13)), and a portion of the gaseous NO molecules were also converted to NO_2 (Reaction (4)) [53]. Hence, the facilitated electron transfer process and abundant adsorbed oxygen species endowed the copper–cobalt spinel catalysts with outstanding soot oxidation activity.

$$C(Soot) + O^* \rightarrow COx + O_v \quad (7)$$

$$Cu^{2+} + Co^{3+} \rightarrow Cu^{+} + Co^{+} + O_{ads} + O_v \quad (8)$$

$$O_{2(gas)} + O_v \rightarrow O_{ads} \quad (9)$$

$$O_{ads} + e^- \rightarrow O_2^- \quad (10)$$

$$O_2^- + e^- \rightarrow O^- \quad (11)$$

$$O^- + e^- \rightarrow O^{2-} \quad (12)$$

$$Cu^{+} + Co^{2+} + O_v \rightarrow Cu^{2+} + Co^{3+} + 2e^- \quad (13)$$

5. Conclusions

To obtain a fundamental understanding on the catalytic soot combustion performance of the $CuCo_2O_4$ catalysts prepared with different metal salt precursors, the relationships between the textural and redox properties of the catalysts and soot conversion were investigated.

(1) The tetragonal spinel crystals of $CuCo_2O_4$ were formed for all catalysts, while the single-metal oxide CuO species was formed only on the $CuCo_2O_4$-N and $CuCo_2O_4$-A catalysts. The $CuCo_2O_4$-N catalysts exhibited a higher specific surface area and well-developed pore structure.

(2) The type of metal precursors could also profoundly affect the redox properties on $CuCo_2O_4$ spinel catalysts. The higher relative content of Co^{3+} (38.4%), Cu^{2+} (51.7%) and O_{ads} (46.8%) species were obtained over the $CuCo_2O_4$-N catalysts. Meanwhile, $CuCo_2O_4$-N catalysts (173 °C) showed a lower reduction temperature over $CuCo_2O_4$-A (184 °C) and $CuCo_2O_4$-C (247 °C). The highest amount of surface adsorbed oxygen species (41.2 $\mu mol \cdot g^{-1}$) was achieved over the $CuCo_2O_4$-N catalysts.

(3) The highest soot conversion activity and CO_2 selectivity were obtained over the $CuCo_2O_4$-N catalysts regardless of the soot combustion conditions. The effects of the contact mode (loose and tight) and NO addition on soot conversion were also investigated. A good correlation between soot conversion and the textural and redox properties of the catalysts were observed. The reaction mechanisms and pathways of the $CuCo_2O_4$ for catalytic soot combustion were also established.

Author Contributions: Conceptualization, X.Z., F.Z. and X.L.; Data curation, C.Z., X.Z. and G.C.; Formal analysis, C.Z., F.Z., X.L., G.C. and G.Y.; Funding acquisition, X.Z.; Investigation, F.Z.; Resources, G.Y.; Supervision, X.Z. and Z.Z.; Validation, Z.Z.; Writing—original draft, C.Z.; Writing—review and editing, X.Z. All authors have read and agreed to the published version of the manuscript.

Funding: This research was funded by National Natural Science Foundation of China (grant No. 51976093).

Institutional Review Board Statement: Not applicable.

Informed Consent Statement: Not applicable.

Data Availability Statement: Not applicable.

Acknowledgments: The authors are grateful for Wentai Wang for the technical support of catalyst characterization and for the experimental platform provided by Ningbo University.

Conflicts of Interest: The authors declare no conflict of interest.

References

1. Choi, M.; Park, S. Optimization of multiple-stage fuel injection and optical analysis of the combustion process in a heavy-duty diesel engine. *Fuel Processing Technol.* **2022**, *228*, 107137. https://doi.org/10.1016/j.fuproc.2021.107137.
2. Jeong, S.; Lee, J.H.; Ha, J.H.; Kim, J.; Kim, I.; Bae, S. An exploratory study of the relationships between diesel engine exhaust particle inhalation, pulmonary inflammation and anxious behavior. *Int. J. Environ. Res. Public Health* **2021**, *18*, 1166. https://doi.org/10.3390/ijerph18031166.
3. Jiaqiang, E.; Zheng, P.; Han, D.; Zhao, X.; Deng, Y. Effects analysis on soot combustion performance enhancement in a rotary diesel particulate filter unit during continuous microwave heating. *Fuel* **2020**, *276*, 118043. https://doi.org/10.1016/j.fuel.2020.118043.
4. Schobing, J.; Tschamber, V.; Brillard, A.; Leyssens, G. Biodiesel soot combustion: Analysis of the soot-catalyst contact in different experimental conditions. *Fuel* **2022**, *312*, 122854. https://doi.org/10.1016/j.fuel.2021.122854.
5. Wang, X.; Jin, B.; Feng, R.; Liu, W.; Weng, D.; Wu, X.; Liu, S. A robust core-shell silver soot oxidation catalyst driven by Co_3O_4: Effect of tandem oxygen delivery and Co_3O_4-CeO_2 synergy. *Appl. Catal. B Environ.* **2019**, *250*, 132–142. https://doi.org/10.1016/j.apcatb.2019.03.019.
6. Shen, J.; Rao, C.; Fu, Z.; Feng, X.; Liu, J.; Fan, X.; Peng, H.; Xu, X.; Tan, C.; Wang, X. The influence on the structural and redox property of CuO by using different precursors and precipitants for catalytic soot combustion. *Appl. Surf. Sci.* **2018**, *453*, 204–213. https://doi.org/10.1016/j.apsusc.2018.05.087.
7. Li, K.; Li, T.; Dai, Y.; Quan, Y.; Zhao, J.; Ren, J. Highly active urchin-like MCo_2O_4 (M=Co, Cu, Ni or Zn) spinel for toluene catalytic combustion. *Fuel* **2022**, *318*, 123648. https://doi.org/10.1016/j.fuel.2022.123648.
8. Lin, C.S.; Liu, H.Y.; Guo, M.; Zhao, Y.H.; Su, X.; Zhang, P.Y.; Zhang, Y.F. Plasmon-induced broad spectrum photocatalytic overall water splitting: Through non-noble bimetal nanoparticles hybrid with reduced graphene oxide. *Colloids Surf. A Physicochem. Eng. Asp.* **2022**, *646*, 128962. https://doi.org/10.1016/j.colsurfa.2022.128962.
9. Fino, D.; Bensaid, S.; Piumetti, M.; Russo, N. A review on the catalytic combustion of soot in Diesel particulate filters for automotive applications: From powder catalysts to structured reactors. *Appl. Catal. A Gen.* **2016**, *509*, 75–96. https://doi.org/10.1016/j.apcata.2015.10.016.
10. Zhang, S.; Zhu, X.; Zheng, C.; Hu, D.; Zhang, J.; Gao, X. Study on catalytic soot oxidation over spinel type ACo_2O_4 (A=Co, Ni, Cu, Zn) catalysts. *Aerosol Air Qual. Res.* **2017**, *17*, 2317–2327. https://doi.org/10.4209/aaqr.2016.12.0564.
11. Jampaiah, D.; Velisoju, V.K.; Venkataswamy, P.; Coyle, V.E.; Nafady, A.; Reddy, B.M.; Bhargava, S.K. Nanowire morphology of mono- and bidoped α-MnO_2 catalysts for remarkable enhancement in soot oxidation. *ACS Appl. Mater. Interfaces* **2017**, *9*, 32652–32666. https://doi.org/10.1021/acsami.7b07656.
12. Zhang, F.; Zhu, X.; Wu, H.; Wu, X.; Zhou, Z.; Chen, G.; Yang, G. Activity and stability of Cu-based spinel-type complex oxides for diesel soot combustion. *ChemistrySelect* **2021**, *6*, 14019–14026. https://doi.org/10.1002/slct.202102899.
13. Okal, J.; Zawadzki, M.; Kraszkiewicz, P.; Adamska, K. Ru/CeO_2 catalysts for combustion of mixture of light hydrocarbons: Effect of preparation method and metal salt precursors. *Appl. Catal. A Gen.* **2018**, *549*, 161–169. https://doi.org/10.1016/j.apcata.2017.09.036.
14. Yang, T.; Zhao, M.; Wang, X.; Ma, R.; Liu, Y.; He, Y.; Li, D. Influence of active metal precursors on the structure and catalytic behavior of Pd/Al_2O_3 catalysts for selective acetylene hydrogenation. *Catal. Lett.* **2021**, *152*, 227–238. https://doi.org/10.1007/s10562-021-03620-w.
15. Wang, Y.; Tao, Z.; Wu, B.; Xu, J.; Huo, C.; Li, K.; Chen, H.; Yang, Y.; Li, Y. Effect of metal precursors on the performance of Pt/ZSM-22 catalysts for n-hexadecane hydroisomerization. *J. Catal.* **2015**, *322*, 1–13. https://doi.org/10.1016/j.jcat.2014.11.004.
16. Yu, Z.; Hu, X.; Jia, P.; Zhang, Z.; Dong, D.; Hu, G.; Hu, S.; Wang, Y.; Xiang, J. Steam reforming of acetic acid over nickel-based catalysts: The intrinsic effects of nickel precursors on behaviors of nickel catalysts. *Appl. Catal. B Environ.* **2018**, *237*, 538–553. https://doi.org/10.1016/j.apcatb.2018.06.020.
17. Liu, H.; Zhuang, M.; Zhang, Z.; Dai, X.; Qian, L.; Yan, Z. Catalytic removal of soot particles over $MnCo_2O_4$ catalysts prepared by the auto-combustion method. *Chem. Pap.* **2018**, *72*, 1973–1979. https://doi.org/10.1007/s11696-018-0397-7.
18. Jin, C.; Cui, Y.; Zhang, G.; Luo, W.; Liu, Y.; Sun, Y.; Tian, Z.; Zheng, W. Synthesis of copper-cobalt hybrid oxide microflowers as electrode material for supercapacitors. *Chem. Eng. J.* **2018**, *343*, 331–339. https://doi.org/10.1016/j.cej.2018.02.117.
19. Lu, J.; Zhong, J.; Ren, Q.; Li, J.; Song, L.; Mo, S.; Zhang, M.; Chen, P.; Fu, M.; Ye, D. Construction of Cu-Ce interface for boosting toluene oxidation: Study of Cu-Ce interaction and intermediates identified by in situ DRIFTS. *Chin. Chem. Lett.* **2021**, *32*, 3435–3439. https://doi.org/10.1016/j.cclet.2021.05.029.

20. Wen, X.; Xu, L.; Chen, M.; Shi, Y.; Lv, C.; Cui, Y.; Wu, X.; Cheng, G.; Wu, C.-E.; Miao, Z.; et al. Exploring the influence of nickel precursors on constructing efficient Ni-based CO_2 methanation catalysts assisted with in-situ technologies. *Appl. Catal. B Environ.* **2021**, *297*, 120486. https://doi.org/10.1016/j.apcatb.2021.120486.
21. Kang, T.; Kim, J. Optimal cobalt-based catalyst containing high-ratio of oxygen vacancy synthesized from metal-organic-framework (MOF) for oxygen evolution reaction (OER) enhancement. *Appl. Surf. Sci.* **2021**, *560*, 150035. https://doi.org/10.1016/j.apsusc.2021.150035.
22. Li, Y.; Han, W.; Wang, R.; Weng, L.-T.; Serrano-Lotina, A.; Bañares, M.A.; Wang, Q.; Yeung, K.L. Performance of an aliovalent-substituted $CoCeO_x$ catalyst from bimetallic MOF for VOC oxidation in air. *Appl. Catal. B Environ.* **2020**, *275*, 119121. https://doi.org/10.1016/j.apcatb.2020.119121.
23. Xiao, S.Y.; Liu, Y.; Wu, X.F.; Gan, L.T.; Lin, H.Y.; Zheng, L.R.; Dai, S.; Liu, P.F.; Yang, H.G. A low-valent cobalt oxide co-catalyst to boost photocatalytic water oxidation via enhanced hole-capturing ability. *J. Mater. Chem. A* **2021**, *9*, 14786–14792. https://doi.org/10.1039/d1ta01858b.
24. Huang, C.; Yu, Y.; Tang, X.; Liu, Z.; Zhang, J.; Ye, C.; Ye, Y.; Zhang, R. Hydrogen generation by ammonia decomposition over Co/CeO_2 catalyst: Influence of support morphologies. *Appl. Surf. Sci.* **2020**, *532*, 147335. https://doi.org/10.1016/j.apsusc.2020.147335.
25. Andana, T.; Piumetti, M.; Bensaid, S.; Veyre, L.; Thieuleux, C.; Russo, N.; Fino, D.; Quadrelli, E.A.; Pirone, R. CuO nanoparticles supported by ceria for NO_x-assisted soot oxidation: Insight into catalytic activity and sintering. *Appl. Catal. B Environ.* **2017**, *216*, 41–58. https://doi.org/10.1016/j.apcatb.2017.05.061.
26. Du, H.; Ma, X.; Jiang, M.; Yan, P.; Conrad Zhang, Z. Highly efficient Cu/SiO_2 catalyst derived from ethanolamine modification for furfural hydrogenation. *Appl. Catal. A Gen.* **2020**, *598*, 117598. https://doi.org/10.1016/j.apcata.2020.117598.
27. Liang, H.; Jin, B.; Li, M.; Yuan, X.; Wan, J.; Liu, W.; Wu, X.; Liu, S. Highly reactive and thermally stable Ag/YSZ catalysts with macroporous fiber-like morphology for soot combustion. *Appl. Catal. B Environ.* **2021**, *294*, 120271. https://doi.org/10.1016/j.apcatb.2021.120271.
28. Xu, Y.; Qu, Z.P.; Ren, Y.W.; Dong, C. Enhancement of toluene oxidation performance over Cu-Mn composite oxides by regulating oxygen vacancy. *Appl. Surf. Sci.* **2021**, *560*, 149983. https://doi.org/10.1016/j.apsusc.2021.149983.
29. Wang, J.; Chernavskii, P.A.; Khodakov, A.Y.; Wang, Y. Structure and catalytic performance of alumina-supported copper-cobalt catalysts for carbon monoxide hydrogenation. *J. Catal.* **2012**, *286*, 51–61. https://doi.org/10.1016/j.jcat.2011.10.012.
30. Jia, A.-P.; Hu, G.-S.; Meng, L.; Xie, Y.-L.; Lu, J.-Q.; Luo, M.-F. CO oxidation over $CuO/Ce_{1-x}Cu_xO_{2-\delta}$ and $Ce_{1-x}Cu_xO_{2-\delta}$ catalysts: Synergetic effects and kinetic study. *J. Catal.* **2012**, *289*, 199–209. https://doi.org/10.1016/j.jcat.2012.02.010.
31. Song, L.; Xiong, J.; Cheng, H.; Lu, J.; Liu, P.; Fu, M.; Wu, J.; Chen, L.; Huang, H.; Ye, D. In-Situ characterizations to investigate the nature of Co^{3+} coordination environment to activate surface adsorbed oxygen for methane oxidation. *Appl. Surf. Sci.* **2021**, *556*, 149713. https://doi.org/10.1016/j.apsusc.2021.149713.
32. Lu, S.; Wang, F.; Chen, C.; Huang, F.; Li, K. Catalytic oxidation of formaldehyde over CeO_2-Co_3O_4 catalysts. *J. Rare Earths* **2017**, *35*, 867–874. https://doi.org/10.1016/s1002-0721(17)60988-8.
33. Yang, Y.; Zhao, D.; Gao, Z.; Tian, Y.; Ding, T.; Zhang, J.; Jiang, Z.; Li, X. Interface interaction induced oxygen activation of cactus-like Co_3O_4/OMS-2 nanorod catalysts in situ grown on monolithic cordierite for diesel soot combustion. *Appl. Catal. B Environ.* **2021**, *286*, 119932. https://doi.org/10.1016/j.apcatb.2021.119932.
34. Cui, B.; Yan, S.; Xia, Y.; Li, K.; Li, S.; Wang, D.; Ye, Y.; Liu, Y.-Q. Cu Ce1-O_2 nanoflakes with improved catalytic activity and thermal stability for diesel soot combustion. *Appl. Catal. A Gen.* **2019**, *578*, 20–29. https://doi.org/10.1016/j.apcata.2019.03.025.
35. He, J.; Yao, P.; Qiu, J.; Zhang, H.; Jiao, Y.; Wang, J.; Chen, Y. Enhancement effect of oxygen mobility over $Ce_{0.5}Zr_{0.5}O_2$ catalysts doped by multivalent metal oxides for soot combustion. *Fuel* **2021**, *286*, 119359. https://doi.org/10.1016/j.fuel.2020.119359.
36. Zhang, Y.; Zeng, Z.; Li, Y.; Hou, Y.; Hu, J.; Huang, Z. Effect of the A-site cation over spinel AMn_2O_4 (A=Cu^{2+}, Ni^{2+}, Zn^{2+}) for toluene combustion: Enhancement of the synergy and the oxygen activation ability. *Fuel* **2021**, *288*, 119700. https://doi.org/10.1016/j.fuel.2020.119700.
37. Zhao, M.; Deng, J.; Liu, J.; Li, Y.; Liu, J.; Duan, Z.; Xiong, J.; Zhao, Z.; Wei, Y.; Song, W.; et al. Roles of surface-active oxygen species on 3DOM cobalt-based spinel catalysts $M_xCo_{3-x}O_4$ (M=Zn and Ni) for NO_x-assisted soot oxidation. *ACS Catal.* **2019**, *9*, 7548–7567. https://doi.org/10.1021/acscatal.9b01995.
38. Geng, Q.; Wang, H.; Wang, J.; Hong, J.; Sun, W.; Wu, Y.; Wang, Y. Boosting the capacity of aqueous Li-ion capacitors via pinpoint surgery in nanocoral-like covalent organic frameworks. *Small Methods* **2022**, *6*, 2200314. https://doi.org/10.1002/smtd.202200314.
39. Feng, F.; Zheng, Y.; Shen, X.; Zheng, Q.; Dai, S.; Zhang, X.; Huang, Y.; Liu, Z.; Yan, K. Characteristics of back corona discharge in a honeycomb catalyst and its application for treatment of volatile organic compounds. *Environ. Sci. Technol.* **2015**, *49*, 6831–6837. https://doi.org/10.1021/acs.est.5b00447.
40. Roberts, C.A.; Paidi, V.K.; Shepit, M.; Peck, T.C.; Stamm Masias, K.L.; van Lierop, J.; Reddy, G.K. Effect of Cu substitution on the structure and reactivity of $Cu_xCo_{3-x}O_4$ spinel catalysts for direct NO_x decomposition. *Catal. Today* **2021**, *360*, 204–212. https://doi.org/10.1016/j.cattod.2020.05.050.
41. Xiong, J.; Wu, Q.; Mei, X.; Liu, J.; Wei, Y.; Zhao, Z.; Wu, D.; Li, J. Fabrication of spinel-type $Pd_xCo_{3-x}O_4$ binary active sites on 3D ordered meso-macroporous Ce-Zr-O_2 with enhanced activity for catalytic soot oxidation. *ACS Catal.* **2018**, *8*, 7915–7930. https://doi.org/10.1021/acscatal.8b01924.
42. Yu, D.; Peng, C.; Yu, X.; Wang, L.; Li, K.; Zhao, Z.; Li, Z. Facile preparation of amorphous $CenMnO_x$ catalysts and their good catalytic performance for soot combustion. *Fuel* **2022**, *307*, 121803. https://doi.org/10.1016/j.fuel.2021.121803.

43. Zhang, W.; Descorme, C.; Valverde, J.L.; Giroir-Fendler, A. Cu-Co mixed oxide catalysts for the total oxidation of toluene and propane. *Catal. Today* **2022**, *384–386*, 238–245. https://doi.org/10.1016/j.cattod.2021.04.005.
44. Ambrogio, M.; Saracco, G.; Specchia, V. Combining filtration and catalytic combustion in particulate traps for diesel exhaust treatment. *Chem. Eng. Sci.* **2001**, *56*, 1613–1621. https://doi.org/10.1016/S0009-2509(00)00389-4.
45. Cao, C.; Xing, L.; Yang, Y.; Tian, Y.; Ding, T.; Zhang, J.; Hu, T.; Zheng, L.; Li, X. The monolithic transition metal oxide crossed nanosheets used for diesel soot combustion under gravitational contact mode. *Appl. Surf. Sci.* **2017**, *406*, 245–253. https://doi.org/10.1016/j.apsusc.2017.02.117.
46. Yeste, M.P.; Cauqui, M.Á.; Giménez-Mañogil, J.; Martínez-Munuera, J.C.; Muñoz, M.Á.; García-García, A. Catalytic activity of Cu and Co supported on ceria-yttria-zirconia oxides for the diesel soot combustion reaction in the presence of NO_x. *Chem. Eng. J.* **2020**, *380*, 122370. https://doi.org/10.1016/j.cej.2019.122370.
47. Chen, Y.; Shen, G.; Lang, Y.; Chen, R.; Jia, L.; Yue, J.; Shen, M.; Du, C.; Shan, B. Promoting soot combustion efficiency by strengthening the adsorption of NO_x on the 3DOM mullite catalyst. *J. Catal.* **2020**, *384*, 96–105. https://doi.org/10.1016/j.jcat.2020.02.006.
48. Zhang, H.; Zhou, C.; Galvez, M.E.; Da Costa, P.; Chen, Y. MnO_x-CeO_2 mixed oxides as the catalyst for NO-assisted soot oxidation: The key role of NO adsorption/desorption on catalytic activity. *Appl. Surf. Sci.* **2018**, *462*, 678–684. https://doi.org/10.1016/j.apsusc.2018.08.186.
49. Martínez-Munuera, J.C.; Zoccoli, M.; Giménez-Mañogil, J.; García-García, A. Lattice oxygen activity in ceria-praseodymia mixed oxides for soot oxidation in catalysed gasoline particle filters. *Appl. Catal. B Environ.* **2019**, *245*, 706–720. https://doi.org/10.1016/j.apcatb.2018.12.076.
50. Chen, L.; Li, T.; Zhang, J.; Wang, J.; Chen, P.; Fu, M.; Wu, J.; Ye, D. Chemisorbed superoxide species enhanced the high catalytic performance of Ag/Co_3O_4 nanocubes for soot oxidation. *ACS Appl. Mater. Interfaces* **2021**, *13*, 21436–21449. https://doi.org/10.1021/acsami.1c03935.
51. Guo, X.; Li, J.; Zhou, R. Catalytic performance of manganese doped CuO-CeO_2 catalysts for selective oxidation of CO in hydrogen-rich gas. *Fuel* **2016**, *163*, 56–64. https://doi.org/10.1016/j.fuel.2015.09.043.
52. Lee, J.H.; Lee, B.J.; Lee, D.-W.; Choung, J.W.; Kim, C.H.; Lee, K.-Y. Synergistic effect of Cu on a Ag-loaded CeO_2 catalyst for soot oxidation with improved generation of active oxygen species and reducibility. *Fuel* **2020**, *275*, 117930. https://doi.org/10.1016/j.fuel.2020.117930.
53. Yang, Q.; Gu, F.; Tang, Y.; Zhang, H.; Liu, Q.; Zhong, Z.; Su, F. A Co_3O_4-CeO_2 functionalized SBA-15 monolith with a three-dimensional framework improves NO_x-assisted soot combustion. *RSC Adv.* **2015**, *5*, 26815–26822. https://doi.org/10.1039/c4ra16832a.